Proton Temperature Anisotropy Variations in Inner Heliosphere Estimated with the First *Parker Solar Probe* Observations

Jia Huang[1] , J. C. Kasper[1,2] , D. Vech[1,3] , K. G. Klein[4] , M. Stevens[2] , Mihailo M. Martinović[4,5] , B. L. Alterman[1,6] ,
Tereza Ďurovcová[7] , Kristoff Paulson[2] , Bennett A. Maruca[8,9] , Ramiz A. Qudsi[8] , A. W. Case[2] , K. E. Korreck[2] ,
Lan K. Jian[10] , Marco Velli[11] , B. Lavraud[12] , A. Hegedus[1] , C. M. Bert[1] , J. Holmes[1] , Stuart D. Bale[13,14,15,16] ,
Davin E. Larson[17] , Roberto Livi[17] , P. Whittlesey[17] , Marc Pulupa[17] , Robert J. MacDowall[18] , David M. Malaspina[3,19] ,
John W. Bonnell[20] , Peter Harvey[20] , Keith Goetz[21] , and Thierry Dudok de Wit[22]

[1] Climate and Space Sciences and Engineering, University of Michigan, Ann Arbor, MI 48109, USA; jiahu@umich.edu
[2] Smithsonian Astrophysical Observatory, Cambridge, MA 02138, USA
[3] Laboratory for Atmospheric and Space Physics, University of Colorado, Boulder, CO, USA
[4] Lunar and Planetary Laboratory, University of Arizona, Tucson, AZ 85719, USA
[5] LESIA, Observatoire de Paris, Universite PSL, CNRS, Sorbonne Universite, Universite de Paris, 5 place Jules Janssen, F-92195 Meudon, France
[6] Department of Applied Physics, University of Michigan, 450 Church St., Ann Arbor, MI 48109, USA
[7] Faculty of Mathematics and Physics, Charles University, Prague, Czech Republic
[8] Department of Physics and Astronomy, University of Delaware, Newark, DE 19716, USA
[9] Bartol Research Institute, University of Delaware, Newark, DE 19716, USA
[10] Heliophysics Science Division, NASA Goddard Space Flight Center, Greenbelt, MD 20771 USA
[11] Department of Earth, Planetary and Space Sciences, University of California, Los Angeles, CA 90095, USA
[12] Institut de Recherche en Astrophysique et Planétologie, CNRS, UPS, CNES, Université de Toulouse, Toulouse, France
[13] Physics Department, University of California, Berkeley, CA 94720-7300, USA
[14] Space Sciences Laboratory, University of California, Berkeley, CA 94720-7450, USA
[15] The Blackett Laboratory, Imperial College London, London, SW7 2AZ, UK
[16] School of Physics and Astronomy, Queen Mary University of London, London E1 4NS, UK
[17] University of California, Berkeley, Berkeley, CA 94720, USA
[18] NASA Goddard SFC, Greenbelt, MD 20771, USA
[19] Astrophysical and Planetary Sciences Department, University of Colorado, Boulder, CO 80309, USA
[20] University of Colorado, Boulder, Boulder, CO 80309, USA
[21] University of Minnesota, Minneapolis, MN 55455, USA
[22] LPC2E, CNRS and University of Orléans, 3A avenue de la Recherche Scientifique, Orléans, France

Abstract

We present a technique for deriving the temperature anisotropy of solar wind protons observed by the *Parker Solar Probe* (*PSP*) mission in the near-Sun solar wind. The radial proton temperature measured by the Solar Wind Electrons, Alphas, and Protons (SWEAP) Solar Probe Cup is compared with the orientation of local magnetic field measured by the FIELDS fluxgate magnetometer, and the proton temperatures parallel and perpendicular to the magnetic field are extracted. This procedure is applied to different data products, and the results are compared and optimum timescales for data selection and trends in the uncertainty in the method are identified. We find that the moment-based proton temperature anisotropy is more physically consistent with the expected limits of the mirror and firehose instabilities, possibly because the nonlinear fits do not capture a significant non-Maxwellian shape to the proton velocity distribution function near the Sun. The proton beam has a small effect on total proton temperature anisotropy owing to its much smaller density relative to the core compared to what was seen by previous spacecraft farther from the Sun. Several radial trends in the temperature components and the variation of the anisotropy with parallel plasma beta are presented. Our results suggest that we may see stronger anisotropic heating as *PSP* moves closer to the Sun, and that a careful treatment of the shape of the proton distribution may be needed to correctly describe the temperature.

1. Introduction

Temperatures perpendicular ($T_{\perp p}$; see Appendix for definitions) and parallel ($T_{\parallel p}$) to the ambient magnetic field (***B***) are one measure of the solar wind's departure from thermal equilibrium. Characterizing such departures is pivotal to understanding the kinetic processes governing the dynamics of the interplanetary medium (Kasper et al. 2002, 2007; Maruca et al. 2012; He et al. 2013; Maruca & Kasper 2013). Temperature anisotropy ($T_{\perp p}/T_{\parallel p} \neq 1$) arises when anisotropic heating and cooling processes act preferentially in one direction (Maruca et al. 2011); such preferential heating is supported by observed departures of $T_{\perp p}/T_{\parallel p}$ from adiabatic predictions in

solar wind observations (Matteini et al. 2007). For an ideal spherical adiabatic expansion with a polytropic index $\gamma = 5/3$, the total proton temperature is expected to decrease with heliocentric distance with an index of $T_p \propto R^{-4/3}$. However, observations suggest a much slower decay rate, implying continual proton heating over extended radial distances (Hellinger et al. 2011). Moreover, assuming that the collisionless solar wind has small heat fluxes and rare interactions (Kasper et al. 2003; Matteini et al. 2013; Perrone et al. 2018), the double-adiabatic equations of state predict that the adiabatic invariants $T_{\perp p}/B$ and $T_{\parallel p}B^2/n_p^2$ should be conserved (Chew et al. 1956). As B and proton density n_p decrease as R^{-2} for a solar wind expanding with constant speed, $T_{\perp p}$ is expected to

decrease with R^{-2} and $T_{\parallel p}$ should be constant. However, *Helios* measurements covering radial distances from 0.3 to 1 au (e.g., Marsch et al. 1982, 1983; Hellinger et al. 2011) showed that these adiabatic invariants are not conserved, with $T_{\perp p}$ decreasing slower and $T_{\parallel p}$ decreasing faster than double-adiabatic predictions, implying both a preferential perpendicular heating and parallel cooling of protons (Hellinger et al. 2011). Additionally, $T_{\perp}/B$, effectively the magnetic moment of the solar wind protons, was found to increase with distance in fast wind instead of being conserved, further indicating that the plasma was being heated preferentially perpendicular to the magnetic field.

As temperature anisotropy departs from unity, anisotropy-driven instabilities such as mirror, ion-cyclotron, parallel, and oblique firehose instabilities arise and act to isotropize the plasma (Gary 1993; Liu et al. 2005, 2007; Maruca et al. 2011). However, the thresholds of these instabilities are different in different conditions (e.g., solar wind, magnetosphere, magnetosheath), and many researchers have tested the constraints of these instabilities (Kasper et al. 2002, and references therein). Gary et al. (2000) studied the constraints from ion-cyclotron instability based on theoretical and numerical methods. Kasper et al. (2003) found that the dominant limit in the large plasma β regime for $T_{\perp p} > T_{\parallel p}$ transitions from the ion-cyclotron to the mirror instability threshold. Using *Wind* measurements of the solar wind, Kasper et al. (2002) demonstrated that the firehose instability serves as a constraint on the proton temperature anisotropies when $T_{\perp p} < T_{\parallel p}$. An extended work using *Wind* data by Hellinger et al. (2006) argued that the oblique instabilities (mirror and oblique firehose instabilities) more effectively constrain the proton temperature anisotropy for slow solar wind (SSW), while the mirror and parallel firehose instabilities probably play a role in limiting the proton core temperature anisotropy for fast wind. Besides, both *Wind* data from 1 au and *Helios* data close to 0.3 au exhibit an anticorrelation between $\beta_{\parallel p}$ and $T_{\perp p}/T_{\parallel p}$ for the proton core population (Marsch et al. 2004; Hellinger et al. 2006). Using Nyquist's instability criterion and by assessing ion sources of free energy, Klein et al. (2017, 2018) found that instabilities are pervasive in the solar wind rather than simply serving as a boundary.

The above results are drawn exclusively from measurements at distances greater than 0.3 au. It is valuable to include near-Sun observations to comprehensively and thoroughly investigate how the temperature components and adiabatic invariants vary with distances from the Sun, and to study the impact of anisotropy-driven instabilities in the solar wind at radial distances below 0.3 au. *Parker Solar Probe* (*PSP*; Fox et al. 2016) is designed to fly into the solar atmosphere, reaching a deepest perihelion at $\sim$9.8 solar radii (R_S) at the end of the mission. Currently, *PSP* has operated through several encounters with the Sun at its initial perihelion of $35.7R_S$, and initial overviews of the solar wind plasma seen during these encounters have been reported (Bale et al. 2019; Kasper et al. 2019). As such, it provides novel data that can constrain the behavior and significance of instabilities to solar wind evolution. In this work, we derive temperature anisotropies from *PSP* observations during the first solar encounter (E1). We present the data and methodology in Sections 2 and 3, respectively. Section 4 shows the temperature variations with distance from the Sun, which may indicate stronger perpendicular heating and parallel cooling effects than previous results.

Section 5 presents the temperature anisotropy variations with $\beta_{\parallel p}$, suggesting that the mirror and parallel firehose instabilities may well constrain the temperature anisotropy of SSW. We summarize our results in Section 6 and present the details of our fitting technique used to derive temperature anisotropies in Appendices A–D.

2. Data

PSP carries the Solar Wind Electrons, Alphas, and Protons (SWEAP) instrument suite (Kasper et al. 2016) and the FIELDS instrument suite (Bale et al. 2016). SWEAP is a thermal ion package designed to measure velocity distributions of solar wind electrons, alpha particles, and protons. The suite includes the Solar Probe Cup (SPC; Case et al. 2020) and Solar Probe Analyzers (SPANs; P. Whittlesey & SWEAP 2019, in preparation; R. Roberto & SWEAP 2019, in preparation). SPC is a Sun-pointed Faraday cup (FC). The SPANs have an A and B component, each consisting of one or more electrostatic analyzers (ESAs). SPAN-A is mounted on the ram side and includes an ion and electron ESA. SPAN-B contains an electron ESA mounted on the anti-ram side. In this paper, we focus on proton measurements derived from SPC. SPC reports proton measurements derived from both *moment* and *nonlinear* fitting algorithms. The *moment* algorithm returns a single, isotropic proton population. The *nonlinear* fitting algorithm returns a proton core and a proton beam population. Typically, the proton core corresponds to the peak of the solar wind proton velocity distribution function (VDF), and the beam corresponds to its shoulder. A summed core+beam population by taking into account their relative drift is also reported. Future SWEAP data products will include measurements of the proton temperature anisotropy using the three-dimensional VDF seen by SPAN-A, but this analysis is under development and *PSP* has yet to achieve a sufficiently large orbital velocity for the peak of the solar wind VDF to be seen by SPAN-A. FIELDS is designed to measure DC and fluctuation magnetic and electric fields, plasma wave spectra and polarization properties, the spacecraft floating potential, and solar radio emissions (Bale et al. 2016).

SPC's operation mode varies with distance from the Sun. During near-Sun encounters ($R < 0.25$ au or $54R_S$), its sampling rate is highest (Kasper et al. 2016). The Encounter mode collected one measurement every 0.874 s in E1 (Case et al. 2020). For nonencounter cruise operations, time resolution is lowered. The Cruise mode collected one solar wind VDF every 27.962 s (Case et al. 2020) during E1. We select intervals for which all the SPC proton quality flags (excepting the four flags associated with helium measurements that are still under calibration) indicate good observations, and the meaning of each quality flag is explained in Case et al. (2020).

PSP/FIELDS collects high-resolution vector magnetic fields with variable time resolution. During E1, the data rates range between 2.3 and 293 Hz (Bale et al. 2019). As these data rates are markedly higher than SPC's, we down-sample the time resolution to that of plasma data for this work.

3. Method

As noted above, there are two techniques to derive plasma parameters from FC measurements: one is a *nonlinear* fitting technique, and the other is a summed *moment* technique
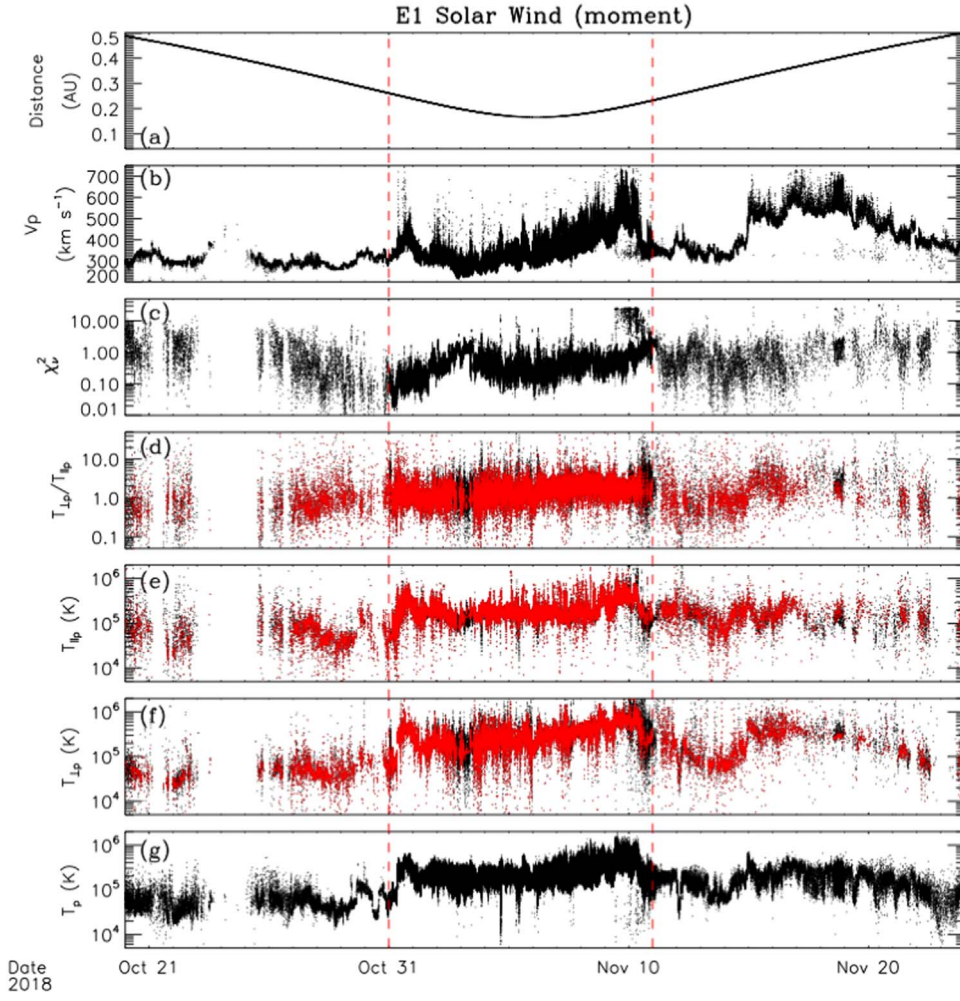
Figure 1. Overview of temperature variations during Encounter 1. From top to bottom, the panels show the spacecraft distance from the Sun, solar wind speed, goodness of fit χ^2_ν, temperature anisotropy, parallel temperature, perpendicular temperature, and total temperature. Red points in panels (d) to (f) indicate good data points selected by our selection criteria as shown in Appendix B. The dashed vertical lines show high time resolution data inside 0.25 au.

(Kasper 2002; Kasper et al. 2006). Kasper (2002) suggests that the *nonlinear* fitting technique provides far more information than the *moment* algorithm, but the *moment* algorithm is used owing to its simplicity, and it provides an easy visualization of the temperature anisotropies.

An anisotropic, magnetized plasma has different thermal speeds parallel ($w_\parallel$) and perpendicular ($w_\perp$) to the local magnetic field. Because an FC measures the reduced VDF and has a very uniform angular response, the instrument reports an effective thermal speed ($\tilde{w}$) that is a function of the orientation between the FC's look direction and the ambient magnetic field (Kasper 2002; Kasper et al. 2002, 2006). For FC look direction $\hat{n}$ and magnetic field direction $\hat{b}$, $\tilde{w}$ is given by

$$\tilde{w} = \sqrt{w_\parallel^2(\hat{n}\cdot\hat{b})^2 + w_\perp^2(1-(\hat{n}\cdot\hat{b})^2)}. \qquad (1)$$

Kasper (2002) applies this equation to *Wind* FC data, which utilize multiple look directions within a single measurement. In contrast, SPC only utilizes a single look direction. During encounter phases of the orbit, this direction is Sun-pointed, i.e., $\hat{n} = \hat{r}$. As such, we can replace $(\hat{n}\cdot\hat{b})^2$ with $(\hat{r}\cdot\hat{b})^2 = (B_r/B)^2$. To apply the *Wind*/FC techniques, we treat successive radial measurements as if they were the multiple FC look directions and combine them with magnetic field measurements

to extract a temperature anisotropy. Appendix B covers the details of our algorithm. Hereafter, our results and analysis utilize the selected temperature anisotropy measurements for total proton population that derived from E1 *moment* data covering the dates 2018 October 20 to November 24. We bin the data with a 1-minute rolling boxcar that steps with 10 s increments and then fit the data in each bin. For the Cruise data, we implement a 4-minute boxcar with a 1-minute moving step. In both cases, the moving step corresponds to the frequency of resulting anisotropy measurements. During this time period, SPC has 1,787,558 measurements in total, of which 1,629,944 (91.2%) are flagged as good observations. The majority of the measurements (1,459,029, 89.5%) are in SSW ($v_{sw} \leqslant 450$ km s^{-1}). The remaining 170,915 (10.5%) measurements are in fast solar wind (FSW, $v_{sw} > 450$ km s^{-1}). Our boxcar algorithm transforms these spectra into 129,586 anisotropy measurements in total, of which 78,499 (60.6%) meet the data quality selection criteria outlined in Appendix B. Among them, SSW dominates 86.2% (67,668 fittings), and FSW dominates the remaining 13.8% (10,831 fittings).

Figure 1 shows an overview of proton temperature variations during E1, including both Encounter and Cruise mode data. High time resolution data inside 0.25 au are from October 31 to November 11 as shown by the dashed vertical lines, and low
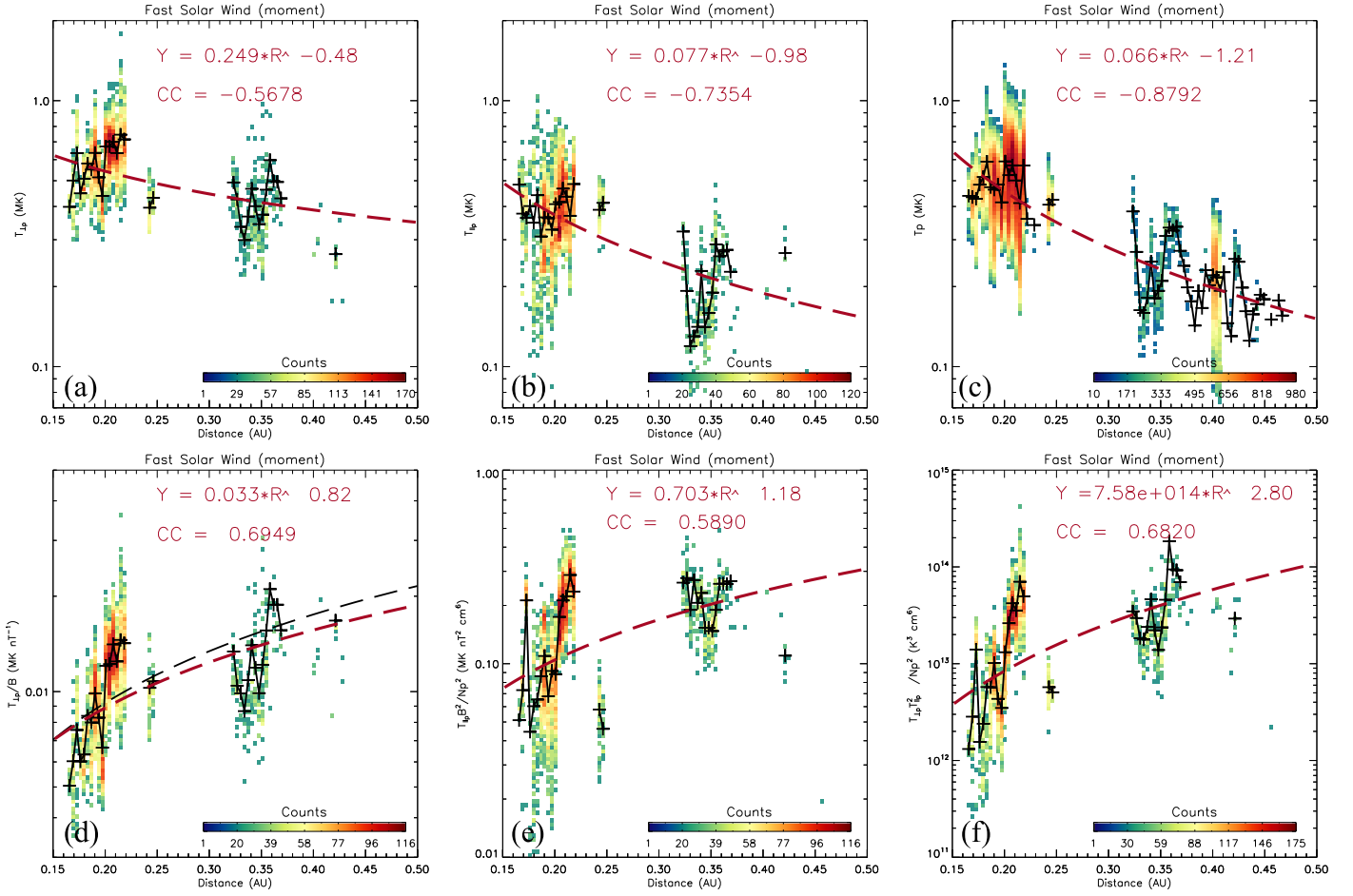
Figure 2. Temperature variations with heliocentric distance for FSW. The top panels show perpendicular temperature $T_{\perp p}$, parallel temperature $T_{\|p}$, and total temperature T_p, and the bottom panels show the double-adiabatic invariants $T_{\perp p}/B$, $T_{\|p}B^2/N_p^2$, and invariant $T_{\|p}T_{\perp p}^2/N_p^2$. Color indicates observation counts. The black crosses in each panel are average values at different bins of heliocentric distance, and the value is calculated when the bin includes at least 30 measurements. Red dashed lines represent the fitted relationships, with the fitted parameters and correlation coefficients present. In panel (d), the black dashed line indicates the *Helios* results adapted from Tu (1988) and Marsch (1991).

time resolution data cover heliocentric distance from 0.25 to about 0.5 au. Kasper et al. (2019) found that protons are 3–4 times hotter than protons with similar solar wind speed at 1 au. Panels (a) and (g) are consistent with their results, showing a decrease in T_p with increasing distance from the Sun. Panel (b) shows the bulk solar wind speed. χ_ν^2 (reduced χ^2 or χ^2 per degree of freedom) in panel (c) measures the goodness of fit, and the fitting is good when this parameter approaches unity (Bevington et al. 1993). Panel (d) presents the temperature anisotropy. The parallel and perpendicular temperatures in panels (e) and (f) show similar variations to the total temperature. The red (black) points in panels (d) through (f) indicate data points that are (not) selected with the criteria present in Appendix B.

4. Temperature Variations with Distance from the Sun

In this section, we investigate the radial variations of temperature components ($T_{\perp p}$, $T_{\|p}$, and T_p) and adiabatic invariants ($T_{\perp p}/B$, $T_{\|p}B^2/n_p^2$, and $T_{\|p}T_{\perp p}^2/n_p^2$) in different solar wind conditions. Take FSW as an example; Figure 2 presents the results for solar wind with bulk speed larger than $450 \, \text{km s}^{-1}$, with the colored and black crosses in each panel indicating the measurement counts and average values for each bin, and with the red dashed line representing the fitted radial

evolutions. Here we use a linear fitting method to fit the logarithm values of both the parameter and heliocentric distance (the latter in au) and present the relationship in exponential format $Y = a(R/R_0)^b$, where R_0 equals 1 au, a is the 1 au intercept, and b is the power-law index. In panel (4), we overlap $T_{\perp p}/B$ variations for solar wind speed ranges from 600 to $700 \, \text{km s}^{-1}$ with *Helios* data between 0.3 and 1 au (black dashed line; the arbitrary coefficient is adapted for convenience to make comparison), indicating good agreement between both results.

Table 1 lists the fitted radial evolution indexes with 1σ uncertainty for each parameter in FSW, SSW, inbound orbit solar wind, and outbound orbit solar wind, respectively. In order to reduce the effect of measurement numbers at different distances, we fit the data with mean values for each bin (e.g., the black crosses in Figure 2), and we calculate the mean value only when the bin includes at least 30 measurements. For comparison, we list the indexes from Marsch et al. (1983), Hellinger et al. (2011), and Perrone et al. (2018), which are derived from *Helios* observations between 0.3 and 1 au, and these works generally focus on FSW with speed larger than 600 km s^{-1}. The inbound orbit predominantly observes SSW, while the outbound orbit mainly observes FSW. Therefore, the indexes for inbound (outbound) orbit and slow (fast) solar wind are somewhat similar.

Table 1
Radial Variation Indexes for Temperature Components and Adiabatic Invariants

Parameter	PSP Data				Helios Data	
	Inbound	Outbound	SSW[a]	FSW[b]	Perrone+2018[c]	Marsch+1983 & Hellinger+2011[d]
T_p	-1.45 ± 0.16	-0.90 ± 0.15	-1.34 ± 0.12	-1.21 ± 0.09	-0.90 ± 0.08	-0.74
$T_{\perp p}$	-2.07 ± 0.17	-0.94 ± 0.27	-1.94 ± 0.15	-0.48 ± 0.13	-0.99 ± 0.08	-0.83
$T_{\parallel p}$	-1.19 ± 0.21	-0.43 ± 0.16	-0.99 ± 0.13	-0.98 ± 0.16	-0.48 ± 0.09	-0.54
$T_{\perp p}/B$	0.14 ± 0.17	0.68 ± 0.24	0.07 ± 0.15	0.82 ± 0.15	0.65 ± 0.08	0.60 ± 0.90 (300–800 km s^{-1})
$T_{\parallel p}B^2/N_p^2$	-2.08 ± 0.44	0.52 ± 0.67	-1.79 ± 0.37	1.18 ± 0.29	0.30 ± 0.20	-0.35 ± 0.18 (400–500 km s^{-1})
						-0.58 ± 0.19 (500–600 km s^{-1})
$T_{\parallel p}T_{\perp p}^2/N_p^2$	-2.69 ± 0.65	1.56 ± 1.08	-1.88 ± 0.65	2.80 ± 0.54	1.60 ± 0.30	0.60 ± 1.20 (400–600 km s^{-1})
						1.8 (300–400 km s^{-1})
N_p	-1.94 ± 0.11	-2.44 ± 0.17	-2.38 ± 0.28	-2.59 ± 0.18	-2.02 ± 0.05	-1.8
B	-1.90 ± 0.07	-1.59 ± 0.06	-1.83 ± 0.06	-1.66 ± 0.06	-1.63 ± 0.03	-1.6

Notes.
[a] SSW: slow solar wind with speed <450 km s^{-1}.
[b] FSW: fast solar wind with speed >450 km s^{-1}.
[c] Perrone+2018: Perrone et al. (2018); they focus on FSW (>600 km s^{-1}) observed by Helios spacecraft.
[d] Hellinger+2011: Hellinger et al. (2011) focus on FSW (>600 km s^{-1}) observed by Helios spacecraft, including indexes for T_p, $T_{\perp p}$, $T_{\parallel p}$, N_p, and B; Marsch+1983: Marsch et al. (1983) provide indexes for $T_{\perp p}/B$, $T_{\parallel p}B^2/N_p^2$, and $T_{\parallel p}T_{\perp p}^2/N_p^2$.

Focusing on FSW, we compare the indexes derived from PSP data and from Helios data. The total magnetic field strength B decreases with an index of about -1.66, which is nearly the same as in Helios observations. However, the plasma density n_p decreases with an index of -2.59, which is much steeper than previous results and the adiabatic expansion index, implying nonspherical expansion geometry or more dynamic interactions closer to the Sun. For total temperature T_p, the index is -1.21, slightly steeper than Helios results. The three parameters have small errors. From this table, it seems that the perpendicular temperature $T_{\perp p}$ and parallel temperature $T_{\parallel p}$ show significant deviations from double-adiabatic theory predictions when close to the Sun. $T_{\perp p}$ decreases with an index of -0.48, about two times slower than Helios observations, while $T_{\parallel p}$ decreases with an index of -0.98, which is about two times faster than previous results. As stated above, theory predicts $T_{\perp p}$ to decrease with R^{-2} and $T_{\parallel p}$ to be conserved; the much larger deviations may imply more significant perpendicular heating and parallel cooling processes inside 0.3 au. Marsch et al. (1983) found that the so-called double-adiabatic invariants are broken because of possible wave−particle interaction or Coulomb collisions. It is not surprising that PSP also observes the same signature. In comparison, $T_{\perp p}/B$ evolves slightly faster with an index of 0.82, $T_{\parallel p}B^2/N_p^2$ increases much faster than Helios measurements with the index 1.18 versus 0.30, and the consequent invariant $T_{\parallel p}T_{\perp p}^2/N_p^2$ reveals the combined difference of the two double-adiabatic invariants. The even more prominent signatures could be caused by the faster decreases of plasma density and the more remarkable deviations of $T_{\perp p}$ and $T_{\parallel p}$ evolution processes. We note that the estimated errors for these parameters are large because of the fact that we have fewer measurements beyond 0.25 au, and our selection criteria also exclude some data points there. With more data in the future, we will be able to better constrain these radial trends.

In contrast to some earlier studies, we use 450 km s^{-1} instead of 600 km s^{-1} to select FSW because PSP observes little solar wind above 600 km s^{-1} (about 0.6% of good measurements) except in spikes during E1 (Kasper et al. 2019), which may also contribute to the discrepancies in Table 1.

However, the FSW we selected is mainly from E1 outbound orbit, and the solar wind speed increases with distances as shown in panel (b) of Figure 1. Thus, we are probably safe to use 450 km s^{-1} when close to the Sun to select fast wind in this work. We also note that the outbound orbit solar wind shows power-law indexes very similar to Helios FSW. However, PSP observes fast, slow, and fast solar wind as it leaves perihelion. Thus, the indexes for outbound solar wind are results of the mix of FSW and SSW, implying that it will be valuable to investigate the evolution of indexes with different solar wind speed criterion in the future.

5. Temperature Anisotropy Variations with Plasma Beta

As anisotropy-driven instabilities limit the departures of temperature anisotropy from unity, it is valuable to investigate whether they still work in the inner heliosphere. In Figure 3, we present the temperature anisotropy ($T_{\perp p}/T_{\parallel p}$) versus parallel plasma beta ($\beta_{\parallel p}$) for different types of solar wind. The red, blue, orange, and green dashed lines represent mirror, ion-cyclotron, parallel firehose, and oblique firehose instabilities, respectively, using the anisotropy-beta inverse relation from Hellinger et al. (2006). The black solid line in each panel indicates the anticorrelation between $T_{\perp p}/T_{\parallel p}$ and $\beta_{\parallel p}$ of the proton core population, which was first derived from FSW with Helios observations by Marsch et al. (2004).

Due to the SSW dominance during E1, the FSW observations in panel (1) only retain a small number of observations (13.8%); however, the anticorrelation matches pretty well with both Wind and Helios results. SSW in panel (2) reveals a large spread of data points, but their temperature anisotropies seem to be well constrained by the mirror and parallel firehose instabilities. It is different from the case of SSW at 1 au, where mirror and oblique firehose instabilities work more effectively (Hellinger et al. 2006). This could be caused by the use of data from only one PSP encounter, and further investigation of the competition between parallel and oblique firehose instabilities when $T_{\perp p} < T_{\parallel p}$ is also needed. Moreover, Alfvénic SSW is prevalent in the inner heliosphere; thus, we also present the variations of high Alfvénic (normalized cross helicity $|\sigma_C| > 0.7$) SSW in panel (3). It seems that high
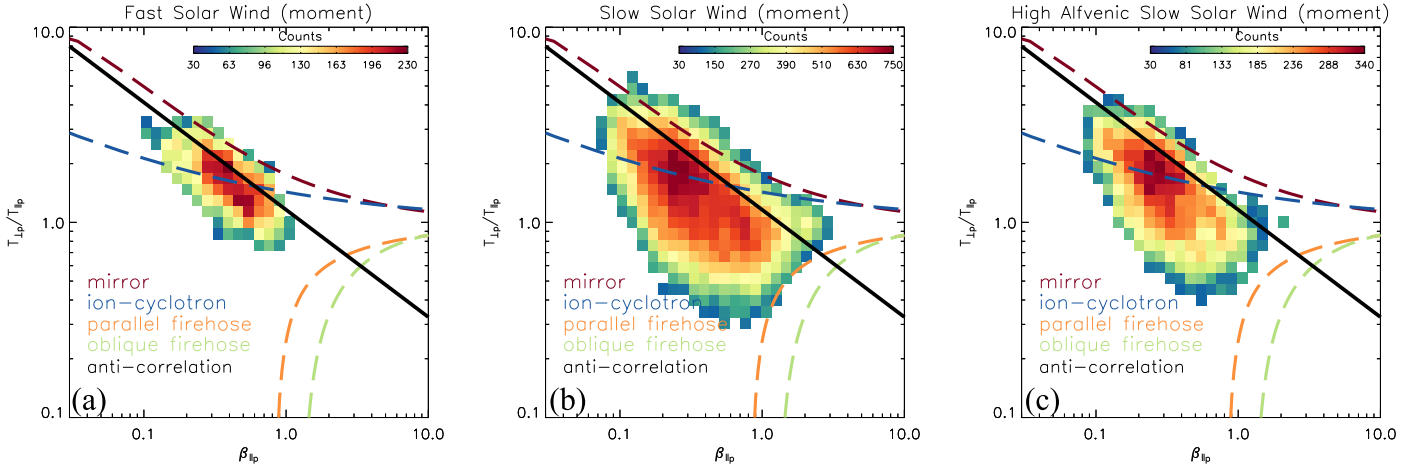
Figure 3. Temperature anisotropy vs. parallel plasma beta in different solar wind. Panels (a)–(c) shows their distributions for FSW, SSW, and high Alfvénic SSW, respectively. The dashed lines are colored to indicate different instabilities with thresholds from Hellinger et al. (2006), and the solid line indicates the anticorrelations derived by Marsch et al. (2004).
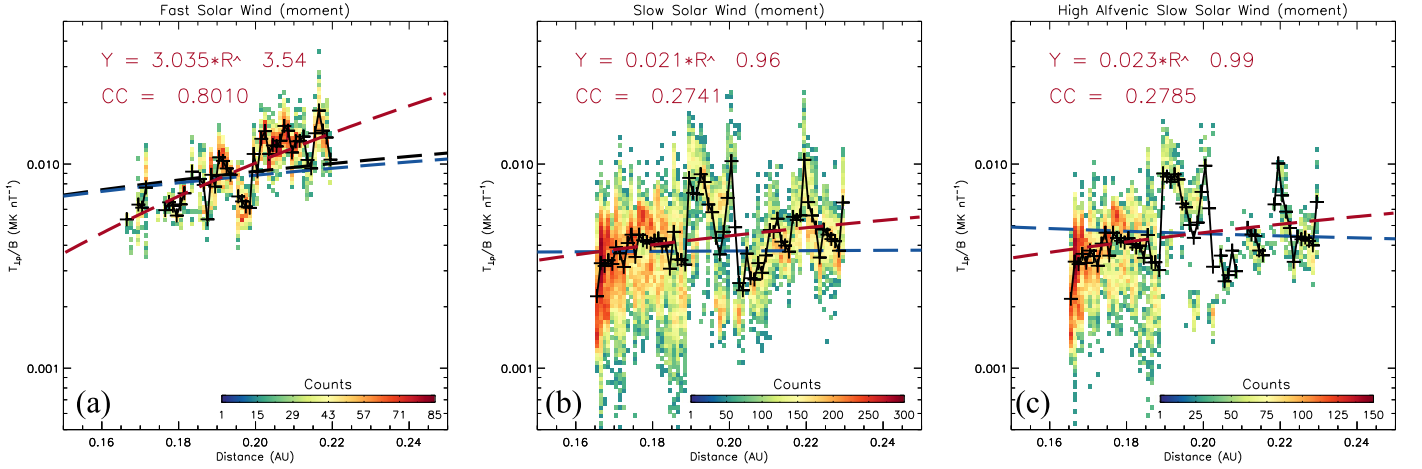

Figure 4. Radial variations of magnetic moment $T_{\perp p}/B$ inside 0.24 au for different solar wind. Panels (a)–(c) shows the variations for FSW, SSW, and high Alfvénic SSW, respectively. The format is similar to Figure 2. The red and blue dashed lines represent fitting results inside 0.24 au and inside 0.50 au, respectively. The black dashed line in panel (a) indicates *Helios* results adapted from Tu (1988) and Marsch (1991).

Alfvénic slow wind has more anisotropic population than regular slow wind, which is similar to FSW. However, the distribution shape may not deviate significantly from slow wind as shown in panel (2).

Figure 3 further suggests that both SSW and FSW show similar trends up against the mirror instability thresholds, while in *Helios* only fast wind does (e.g., Matteini et al. 2007, 2013). Generally, more Coulomb collisions could wash out the anisotropy of SSW plasma (e.g., Marsch & Goldstein 1983; Kasper et al. 2008); thus, the result may imply that *PSP* flies closer into the region where both the slow wind and fast wind experience anisotropic heating. Figure 4 zooms in on the radial variations of magnetic moment $T_{\perp p}/B$ inside 0.24 au. Similar to Figure 2, we present the fitting results inside 0.24 au with red lines and overlap the blue curves that derived from inside 0.5 au. Panel (1) shows that the radial evolution in longer distances (blue line) matches well with *Helios* results (black line) for FSW, but fast wind inside 0.24 au experiences much stronger perpendicular heating, with the magnetic moment increasing to an index of 3.5. For SSW as shown in panels (2) and (3), we also see stronger perpendicular heating compared to outside 0.24 au, but weaker than for the FSW, which is consistent with

our expectations. Instead of the slow wind magnetic moment being essentially flat with distance, from $35R_S$ to $52R_S$ it is observed to increase nearly linearly with distance. This is much weaker than the rapid increase in the FSW magnetic moment, but it suggests that slow wind is also experiencing perpendicular heating close to the Sun. Both regular SSW and Alfvénic SSW show a magnetic moment growing with distance, suggesting that the presence of intense Alfvén waves in the fast wind and the highly Alfvénic slow wind are not solely required for perpendicular heating.

6. Conclusion

In this work, we estimate the temperature anisotropy of solar wind protons observed by the *PSP* mission in the near-Sun solar wind. The components of the proton temperature parallel and perpendicular to the ambient magnetic field are derived by comparing the variation in the temperature of solar wind protons in the radial direction measured by the *PSP*/SWEAP SPC with the variation in the orientation of the local magnetic field measured by the *PSP*/FIELDS fluxgate magnetometer. This algorithm is applied to moments of the proton VDF and to the results of a nonlinear fit of proton core and proton beam

Maxwellian components of the VDF, and the results are compared and optimum timescales for data selection and trends in the uncertainty in the method are identified. We find that the moment-based proton temperature anisotropy is more physically consistent with the expected limits of the mirror and firehose instabilities, possibly because the fits do not capture a significant non-Maxwellian shape to the proton VDF near the Sun. The density of proton beam seems to be only several percent of proton core density, indicating its small contribution to the total proton temperature anisotropies. We also find that the proton parallel plasma beta seen by *PSP* in the first encounter is not significantly smaller than the values seen by *Helios* further from the Sun, possibly as a result of long-term variation in the heliospheric density and magnetic field over the past half century. The radial trends in the temperature components and the variation of the temperature anisotropy with parallel plasma beta are investigated. The results suggest that the radial perpendicular and parallel temperatures in FSW decrease with power-law indexes of -0.48 and -0.98, respectively, implying stronger perpendicular heating and parallel cooling than previous results from *Helios* measurements made at larger radial distances, and a similar anticorrelation between proton temperature anisotropy and parallel plasma beta persists closer to the Sun. However, the mirror and parallel firehose instabilities seem to work as upper and lower limits to constrain the temperature anisotropy of SSW. The perpendicular heating of the SSW inside 0.24 au may contribute to it reaching the mirror instability threshold. The prominent perpendicular heating could be a consequence of the stochastic heating process as confirmed by Martinović et al. (2020). These results suggest that we may see stronger anisotropic heating as *PSP* moves closer to the Sun and that a careful treatment of the shape of the proton VDF may be needed to correctly describe the temperature.

Appendix A
Parameters

Subscripts $\perp$ and $\parallel$ represent the perpendicular and parallel directions, respectively, with respect to ambient magnetic field $\boldsymbol{B}$. T_p, n_p, B_r, and R are the total proton temperature, proton number density, radial component of magnetic field, and heliocentric distance, respectively. $T_{\perp p}$ and $T_{\parallel p}$ are the perpendicular and parallel proton temperatures, respectively. $T_{\perp p}/T_{\parallel p}$ is the proton temperature anisotropy, and $\beta_{\parallel p} = 2\mu_0 n_p k_B T_{\parallel p}/B^2$ is the parallel plasma beta, where μ_0 and k_B denote the vacuum magnetic permeability and Boltzmann

constant, respectively. We use χ_ν^2, i.e., reduced χ^2, to measure goodness of fit, which implies good fitting when it approaches 1 (Bevington et al. 1993).

Appendix B
Selection Method

Due to the SPC data having a variable time resolution, we need to find the best-fitting window and moving step (i.e., the time resolution of fitted temperature anisotropy data) for high and low time resolution data, respectively.

We first choose high time resolution data from 2018 October 31 to November 11 for study. We derive 11 data sets for comparison. Six data sets are of 10 s time resolution, and the fitting window changes from 10 s, 20 s, 30 s, ..., to 60 s. The other five data sets are derived with a 1-minute moving step, and the fitting window includes steps of 1 minute, 3 minutes, 5 minutes, 7 minutes, and 9 minutes. For each data set, if we have sufficient fittings and if we have selected the best timescale to fit the data, then the fitting results should be independent of the spread of data points $(\Delta(B_r/B)^2)$ in each fitting window according to Equation (1). Thus, a uniform distribution of mean temperature anisotropy values ($\langle T_{\perp p}/T_{\parallel p}\rangle$) with $\Delta(B_r/B)^2$ is expected. We have 95,034 fittings for data sets with a 10 s moving step and 15,839 fittings for those with a 1-minute moving step. The left histogram plot in Figure 5 shows the $\langle T_{\perp p}/T_{\parallel p}\rangle$ variations with $\Delta(B_r/B)^2$ in 30 bins for the 11 data sets, and it is obvious that some data sets show more uniform distributions. However, the $\langle T_{\perp p}/T_{\parallel p}\rangle$ value is much larger for each data set when $\Delta(B_r/B)^2$ is very small, which is reasonable because the fitting result could be arbitrary when the data points significantly concentrate together, implying that a minimum $\Delta(B_r/B)^2$ should be applied to select good fittings. In order to find the most uniform distributions, we compare the rms value of $\langle T_{\perp p}/T_{\parallel p}\rangle$ in 30 bins for each data set in the right panel, and we exclude the unusually large value in the first histogram bin during calculations. The results predominantly show a decreasing trend for 10 s time resolution data sets (diamonds) and an increasing trend for 1-minute time resolution data sets (plus signs), and the minimum values for the two different time resolution data sets meet at the 1-minute fitting window. Therefore, the 1-minute fitting window could be the best. This suggests that 1 minute may be a good timescale to estimate temperature anisotropy before the solar wind condition changes. Then, we use the 1-minute fitting window to derive six data sets with moving step changes from 10 to 60 s. According to our analysis (not shown), there is no significant difference between the fitting results, which may also imply that we have probably selected a good timescale to estimate the temperature anisotropy. We would like to set the moving step as 10 s to increase the time resolution of temperature anisotropy data, and it is possible to further increase its time resolution. Consequently, we select the data set fitted with a 1-minute window and a 10 s moving step for further study. For the specific data set, we further require χ_ν^2 smaller than 1 and $\Delta(B_r/B)^2$ larger than, at least, 0.05 to exclude bad fittings. We can use more strict thresholds to select the data, but it seems that the results are not significantly affected.

The Cruise science mode data have a lower time resolution of 27.962 s, i.e., two measurements in 1 minute, so we need to use a larger fitting window to include enough data points but also choose a similar timescale to that we use to fit Encounter
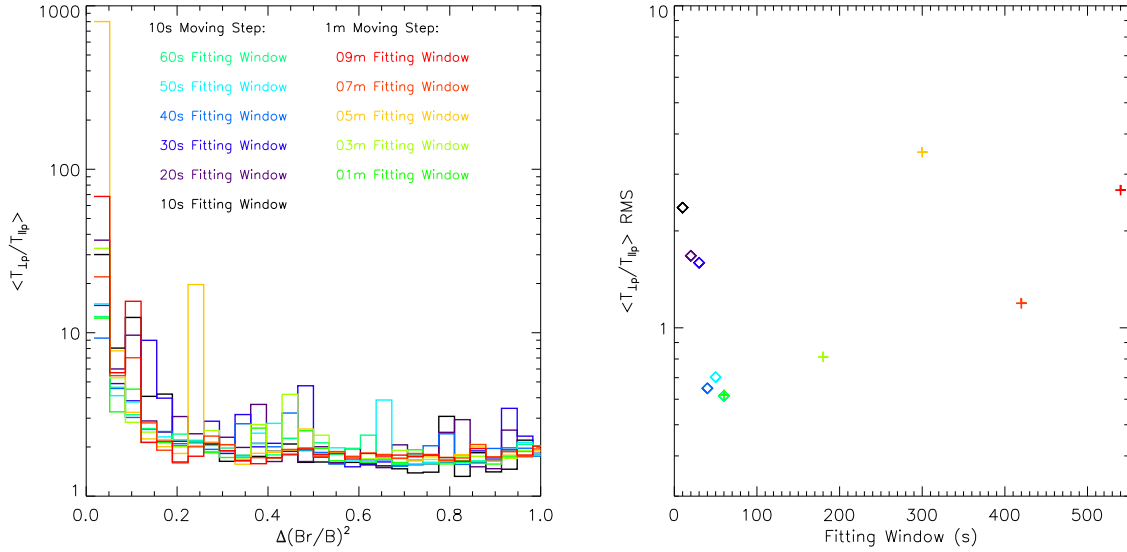
Figure 5. Goodness-of-fit comparison. The left panel shows the average temperature anisotropy ($\langle T_{\perp p}/T_{\parallel p}\rangle$) variations with $\Delta(B_r/B)^2$, and different colors represent data sets derived from different fitting windows and moving steps. The right panel shows the rms of average temperature anisotropy for each data set as indicated by the color, with the diamonds indicating 10 s moving step data sets and plus signs indicating 1-minute moving step data sets.

science mode data. We require the fitting window to include at least six data points, and at least two data points are changed when it moves to the next step. Thus, for the low time resolution data from 2018 October 20 to 31 and from 2018 November 11 to 24, we use the 1-minute moving step to derive nine data sets with the fitting window varying from 4 minutes, 6 minutes, ..., to 20 minutes, and one more data set with a 3-minute fitting window. The comparison (not shown, similar to Figure 5) suggests that a 4-minute fitting window could be better, but these data sets generally show less uniform distributions when compared with data sets derived from high time resolution data. The same χ_ν^2 and $\Delta(B_r/B)^2$ values are applied to remove bad fittings.

In conclusion, for E1 data from 2018 October 20 to November 24, (1) the temperature anisotropy data are relatively better fitted with a 1-minute fitting window and a 10 s moving step for Encounter mode data and a 4-minute fitting window and a 1-minute moving step for Cruise mode data, and (2) the χ_ν^2 smaller than 1 and $\Delta(B_r/B)^2$ larger than 0.05 are necessary to polish the fittings.

Appendix C
Temperature Uncertainty Estimations

Kasper et al. (2006) present the first uncertainty estimations for parallel and perpendicular temperature with a technique that is independent of the method used to extract an estimate of the anisotropy from the raw data. They found that the maximum parallel temperature uncertainty occurs predominantly when the magnetic field is out of the ecliptic plane or perpendicular to the Sun–Earth line, and the perpendicular temperature is poorly constrained when the magnetic field is radial. We note that their method relies on there being a statistically significant sample of observations at high plasma beta above 10, which is not the case for the *PSP* data set. However, it is valuable to estimate the uncertainty based on our linear fitting method and check whether our method could capture the systematic distribution features.

According to Equation (1), the linear fittings will return 1σ uncertainty for both $(T_{\parallel p} - T_{\perp p})$ and $T_{\perp p}$. Therefore, we can directly estimate the uncertainty for $T_{\perp p}$ but need to calculate the propagated uncertainty for $T_{\parallel p}$, implying that its uncertainty would partially include contributions from $T_{\perp p}$. Figure 6 shows the temperature uncertainty distributions with azimuthal angle ϕ_B and elevation angle θ_B. The black lines indicate 10%, 30%, 50%, and 70% measurement contours, and it clearly shows that most of the measurements are clustered at around $\phi_B \sim 160°$, which is nearly the Parker spiral angle of magnetic field at *PSP*'s location. Panel (1) shows the $T_{\perp p}$ median uncertainty distributions, with a mean value of 15.7% and a median value of 7.4%, and about 15% of the data have an uncertainty larger than 50%. This is consistent with the Kasper et al. (2006) result that large $T_{\perp p}$ uncertainty mainly occurs in the radial magnetic field direction. Moreover, the uncertainty is generally larger in the outward direction than in the inward direction, which may be caused by spikes in the outward direction (Kasper et al. 2019). Panel (2) presents the $T_{\parallel p}$ median propagated uncertainty distributions, with a mean value of 82.0% and a median value of 47.4%, and about 48% of the data have an uncertainty larger than 50%. The overall larger $T_{\parallel p}$ uncertainty is partly contributed by $T_{\perp p}$ uncertainty, and it is difficult to accurately calculate the propagated uncertainty of temperature anisotropy. In order to highlight the $T_{\parallel p}$ uncertainty distributions, we compare the ratio between $T_{\parallel p}$ uncertainty and $T_{\perp p}$ uncertainty in panel (3), which indicates the same distributions as suggested by Kasper et al. (2006). The consistency of temperature uncertainty distributions between the two methods, which is not a direct comparison between the results derived from both methods because we cannot apply the *nonlinear* method to SPC data, implies that our method is reliable within the window of provided uncertainties. Besides, we can further exclude fittings with large uncertainties according to the uncertainty distributions, even though only a small fraction of the measurements have large uncertainties as the contours suggest.
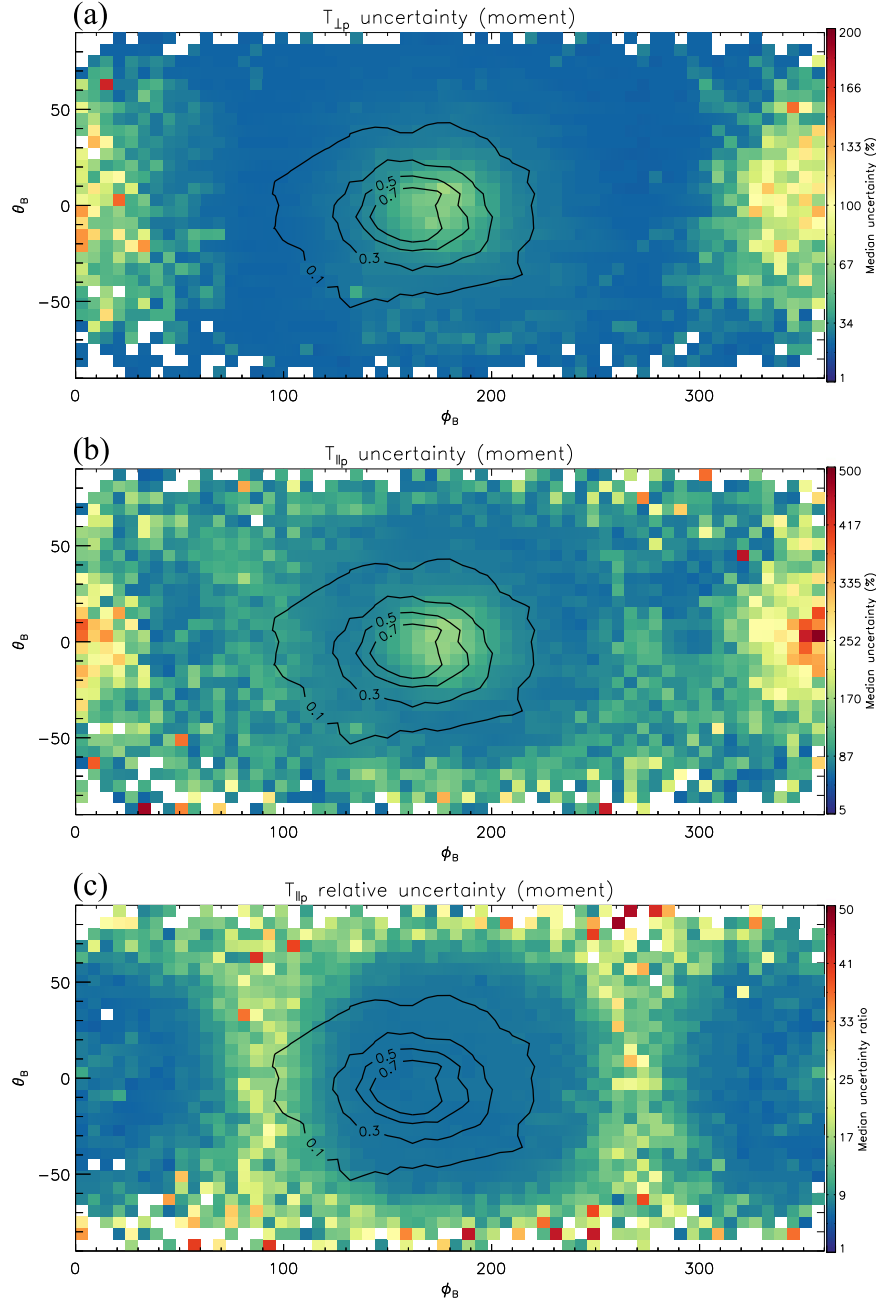
Figure 6. Uncertainty distributions of temperature components. Panels (a) and (b) show perpendicular and parallel temperature uncertainty distributions with azimuthal angle ϕ_B and elevation angle θ_B, respectively. Panel (c) highlights parallel temperature uncertainty by comparing parallel temperature uncertainty in panel (b) with perpendicular temperature uncertainty in panel (a). The black lines indicate 10%, 30%, 50%, and 70% measurement contours.

Appendix D
Temperature Anisotropy Comparisons

For proton data, core, beam, core+beam, and moment data are extracted from SPC measurements (Case et al. 2020), and we fitted the temperature anisotropy for all of them with the method described above. Figure 7, however, only shows the temperature anisotropy versus parallel plasma beta plots for core+beam and moment in panel (1) and panel (2), respectively. We note that the instability constraints are calculated for the total proton population assuming that the temperature anisotropy can be described as a single bi-Maxwellian VDF, while it is hard to derive a single set of instability for combined core and beam populations owing to

the large numbers of multi-ion parameters (Matteini et al. 2013). Thus, we just repeat the same single bi-Maxwellian instability constraints in the core+beam plots for reference under the assumption that we can calculate a total effective parallel and perpendicular temperature by combining the individual fits to the core and beam. Panel (2) shows the overall distributions, which are a combination of SSW and FSW as shown in Figure 3. The distributions for the core+beam population in panel (1) are expected to be similar to the moment results, which do not separate proton populations. We also note that the core+beam temperature components are derived with our linear fitting method from the core+beam data set, which provides the effective total temperature by merging best fits of
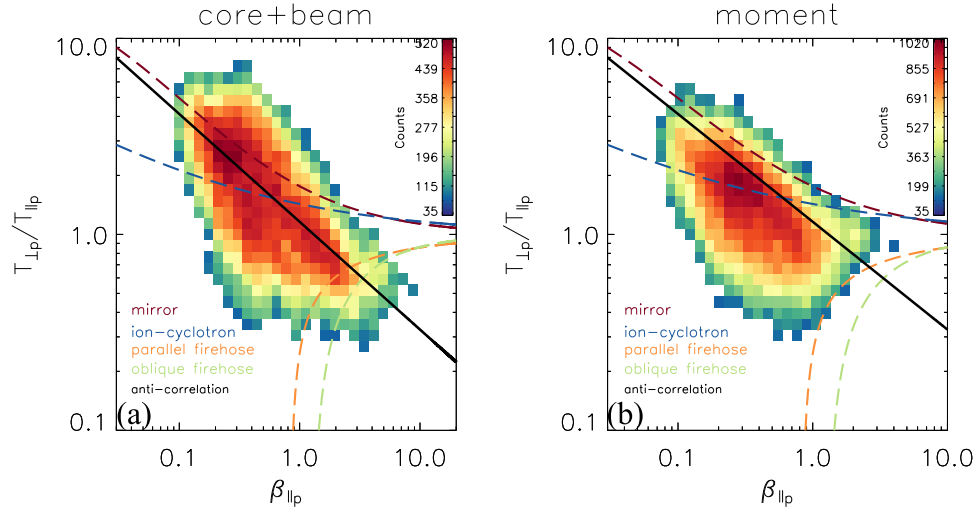
Figure 7. Temperature anisotropy distributions. Panels (a) and (b) show plots for the core+beam and moment population, respectively.
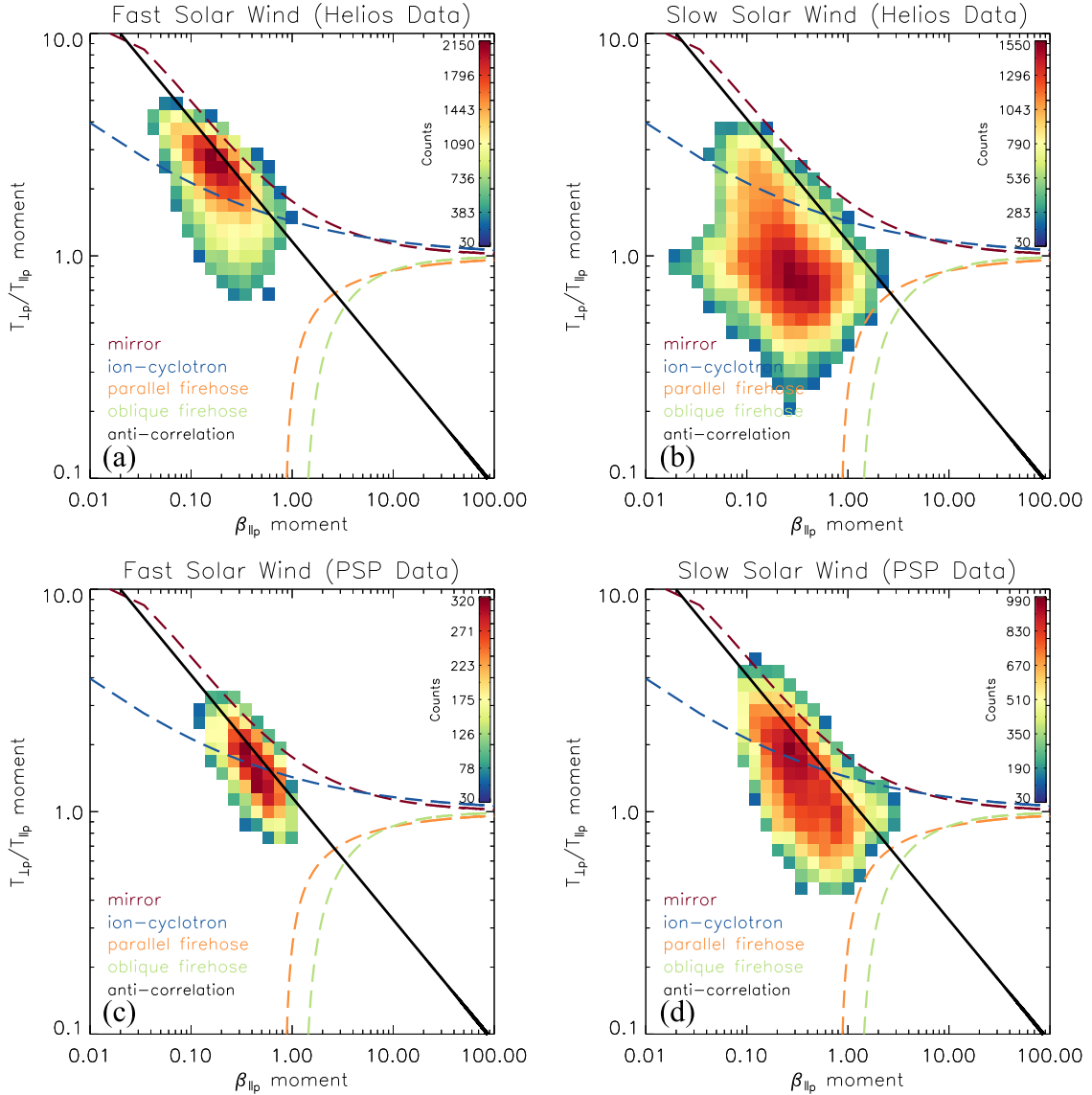

Figure 8. Comparison of temperature anisotropy distributions in different solar winds. Panels (a) and (b) show FSW and SSW distributions, respectively, with *Helios* moment measurements from about 0.30 to 0.35 au. Panels (c) and (d) show FSW and SSW distributions, respectively, with *PSP* moment observations inside 0.25 au during E1.
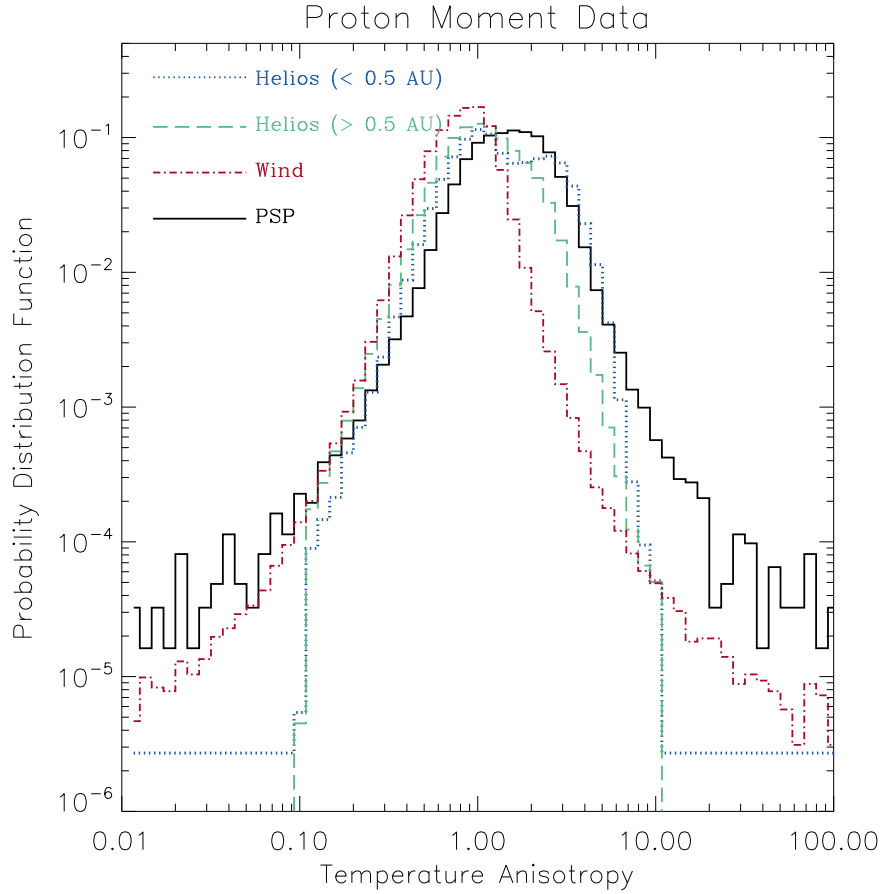
Figure 9. Probability distributions of proton moment temperature anisotropy with different spacecraft observations. The black solid line, red dashed–dotted line, blue dotted line, and green dashed line represent *PSP* data, *Wind* data, *Helios* data inside 0.5 au, and *Helios* data outside 0.5 au, respectively.

core and beam temperatures plus a term due to their relative drift.[23] However, it seems that the moment temperature anisotropies are more physical than those of the core+beam population, which may include systematic errors on parallel temperature estimations due to the core fits not working at low B_r. The core population shows similar distributions to the core+beam population, partly because the beam seems to be only several percent (median value is 6.16%) of the core density and they do not yet appear to be reliable. This is one reason why we primarily show the moment results in this work. Kasper et al. (2006) suggest that the temperature components derived with the moment method could deviate from *nonlinear* results by about 23%. But we cannot apply the *nonlinear* fitting method to SPC data because SPC measures one-dimensional reduced VDF, and the moment method could be a choice to deal with a single ion spectrum. Besides, we think that, if anything, the moment uncertainties on *PSP*/SPC should be lower because the VDF is wider generally and resolved into more energy windows. The more gradually the VDF varies over the energy windows of the plasma instrument and the more windows the VDF is detected in at high signal-to-noise ratio, the more accurate the resulting moments. In addition, we think that

the moment-derived temperature values could be more physical because they do not impose the assumption of a Maxwellian shape on the VDFs. Other studies of the proton VDFs seen by *PSP* are reporting a significant non-Maxwellian kurtosis near E1 perihelion (Martinović et al. 2020) and other significant deviations from the two-Maxwellian model (Case et al. 2020). This implies that different model functions other than bi-Maxwellian (e.g., Wilson et al. 2019a, 2019b found that bi-Kappa works better to fit electron halo and strahl VDFs) might be considered in future work.

In Figure 8, we compare the temperature anisotropy distributions in FSW and SSW between *Helios* and *PSP* results, with the instability constraints overlaid for reference. In order to compare with the total proton results, we calculate *Helios* total proton (moment) parameters with current released core and beam results fitted with the *nonlinear* method by taking into account drift for the parallel component. The *Helios* data from both *Helios* spacecraft below 0.35 au are used to facilitate our comparison with *PSP* moment results inside 0.25 au. The *Helios* 1 data cover late 1974–1985, and the *Helios* 2 data cover 1976–1980. Panels (1) and (3) indicate strong anisotropies in fast wind measured by both spacecraft, and they match well with the anticorrelation line. Further, it seems that *Helios* observe higher temperature anisotropies in smaller parallel beta regions than *PSP* does. The lower *PSP* temperature anisotropies could be caused by the *PSP* observing fast wind with lower speed than *Helios*, and larger parallel beta may be associated with higher parallel temperature than expected in the inner heliosphere. An

---

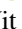[23] The core+beam effective thermal speed is calculated with equation

$$w^2_{\text{core}+\text{beam}} = w^2_{\text{core}} \frac{n_{\text{core}}}{n_{\text{core}} + n_{\text{beam}}} + w^2_{\text{beam}}$$
$$\times \frac{n_{\text{beam}}}{n_{\text{core}} + n_{\text{beam}}} + (v_{\text{core}} - v_{\text{beam}})^2 \frac{n_{\text{core}} n_{\text{beam}}}{(n_{\text{core}} + n_{\text{beam}})^2}.$$

additional explanation for the higher values of parallel beta seen by *PSP* than *Helios* is that the overall strength of the coronal magnetic field has been decreasing over the past 50 yr (Richardson et al. 2002; Janardhan et al. 2015). However, both spacecraft observe that the temperature anisotropies show a trend to mirror thresholds. Moreover, the *PSP* slow wind (panel (4)) is more anisotropic than the *Helios* ones (panel (2)). The difference in slow wind observations may be a consequence of stronger perpendicular temperature heating inside 0.24 au, or the limited data of the *PSP* observations.

In Figure 9, we further compare the probability distribution functions (pdf's) of temperature anisotropies measured by *PSP*, *Helios*, and *Wind* spacecraft. Here we use the *Helios* total proton data from about 0.3 to 1 au with data described above. The *Wind* data are collected at 1 au since 2004 June with *Wind*/SWE Faraday cups (Ogilvie et al. 1995), and the temperature anisotropies are also derived with the *nonlinear* method. The red dashed–dotted line indicates the *Wind* anisotropies, with a median value of 0.78 and a mean value of 0.83. In comparison, *PSP* moment shows nearly two times larger temperature anisotropies when close to the Sun, with a median value and mean value of 1.39 and 1.61, respectively. This could be reasonable if the solar wind experiences stronger anisotropic heating closer to the Sun (Chew et al. 1956; Chandran et al. 2011; Hellinger et al. 2011; Kasper et al. 2017; Stansby et al. 2019). Moreover, we compare them with the *Helios* results inside (blue dotted line) and outside (green dashed line) 0.5 au. The distributions indicate one peak characterized by an isotropic signature that is independent with distances, which could be contributed predominantly by SSW. In contrast to the *Wind* results, *Helios* observations are bimodal and the second peak is more significant at small radial distances, which is consistent with the temperature anisotropy evolution of FSW (e.g., Matteini et al. 2013). Thus, the pdf distribution of *PSP* temperature anisotropies seems to be an average of both peaks, which could be a consequence of two reasons. On one hand, the *PSP* observes rare FSW with speed larger than $600 \, \mathrm{km \, s^{-1}}$; thus, the second anisotropic peak is not that significant. On the other hand, *PSP* observes that solar wind in the inner heliosphere may experience stronger perpendicular heating, so the isotropic peak moves to larger values. Besides, the similar pdf distributions between *PSP* and *Wind*/*Helios* results may further suggest that the *PSP* moment results are reasonable.

ORCID iDs

Jia Huang (ORCID) https://orcid.org/0000-0002-9954-4707
J. C. Kasper (ORCID) https://orcid.org/0000-0002-7077-930X
D. Vech (ORCID) https://orcid.org/0000-0003-1542-1302
K. G. Klein (ORCID) https://orcid.org/0000-0001-6038-1923
M. Stevens (ORCID) https://orcid.org/0000-0002-7728-0085
Mihailo M. Martinović (ORCID) https://orcid.org/0000-0002-7365-0472
B. L. Alterman (ORCID) https://orcid.org/0000-0001-6673-3432
Tereza Ďurovcová (ORCID) https://orcid.org/0000-0003-4247-4864
Kristoff Paulson (ORCID) https://orcid.org/0000-0002-5699-090X
Bennett A. Maruca (ORCID) https://orcid.org/0000-0002-2229-5618
Ramiz A. Qudsi (ORCID) https://orcid.org/0000-0001-8358-0482
A. W. Case (ORCID) https://orcid.org/0000-0002-3520-4041
K. E. Korreck (ORCID) https://orcid.org/0000-0001-6095-2490
Lan K. Jian (ORCID) https://orcid.org/0000-0002-6849-5527
Marco Velli (ORCID) https://orcid.org/0000-0002-2381-3106
B. Lavraud (ORCID) https://orcid.org/0000-0001-6807-8494
A. Hegedus (ORCID) https://orcid.org/0000-0001-6247-6934
C. M. Bert (ORCID) https://orcid.org/0000-0002-9694-174X
Stuart D. Bale (ORCID) https://orcid.org/0000-0002-1989-3596
Davin E. Larson (ORCID) https://orcid.org/0000-0001-5030-6030
Roberto Livi (ORCID) https://orcid.org/0000-0002-0396-0547
P. Whittlesey (ORCID) https://orcid.org/0000-0002-7287-5098
Marc Pulupa (ORCID) https://orcid.org/0000-0002-1573-7457
Robert J. MacDowall (ORCID) https://orcid.org/0000-0003-3112-4201
David M. Malaspina (ORCID) https://orcid.org/0000-0003-1191-1558
Thierry Dudok de Wit (ORCID) https://orcid.org/0000-0002-4401-0943

References

Bale, S., Goetz, K., Harvey, P., et al. 2016, SSRv, 204, 49
Bale, S. D., Badman, S. T., Bonnell, J. W., et al. 2019, Natur, 576, 237
Bevington, P. R., Robinson, D. K., Blair, J. M., Mallinckrodt, A. J., & McKay, S. 1993, ComPh, 7, 415
Case, A. W., Kasper, J. C., Stevens, M. L., et al. 2020, ApJS, doi:10.3847/1538-4365/ab5a7b
Chandran, B. D., Dennis, T. J., Quataert, E., & Bale, S. D. 2011, ApJ, 743, 197
Chew, G., Goldberger, M., & Low, F. 1956, RSPSA, 236, 112
Fox, N., Velli, M., Bale, S., et al. 2016, SSRv, 204, 7
Gary, S. P. 1993, Theory of Space Plasma Microinstabilities No. 7 (Cambridge: Cambridge Univ. Press)
Gary, S. P., Yin, L., & Winske, D. 2000, GeoRL, 27, 2457
He, J., Tu, C., Marsch, E., Bourouaine, S., & Pei, Z. 2013, ApJ, 773, 72
Hellinger, P., Matteini, L., Štverák, Š, Trávníček, P. M., & Marsch, E. 2011, JGRA, 116, A09105
Hellinger, P., Trávníček, P., Kasper, J. C., & Lazarus, A. J. 2006, GeoRL, 33, 9101
Janardhan, P., Bisoi, S. K., Ananthakrishnan, S., et al. 2015, JGRA, 120, 5306
Kasper, J., Lazarus, A., & Gary, S. 2008, PhRvL, 101, 261103
Kasper, J., Lazarus, A., Gary, S., & Szabo, A. 2003, in Proc. AIP 679, SOLAR WIND TEN, ed. M. Velli et al. (Melville, NY: AIP), 538
Kasper, J., Lazarus, A., Steinberg, J., Ogilvie, K., & Szabo, A. 2006, JGRA, 111, 3105
Kasper, J. C. 2002, PhD thesis, Massachusetts Inst. Tech.
Kasper, J. C., Abiad, R., Austin, G., et al. 2016, SSRv, 204, 131
Kasper, J. C., Bale, S. D., Belcher, J. W., et al. 2019, Natur, 576, 228
Kasper, J. C., Klein, K. G., Weber, T., et al. 2017, ApJ, 849, 126
Kasper, J. C., Lazarus, A. J., & Gary, S. P. 2002, GeoRL, 29, 20
Kasper, J. C., Stevens, M. L., Lazarus, A. J., Steinberg, J. T., & Ogilvie, K. W. 2007, ApJ, 660, 901
Klein, K., Alterman, B., Stevens, M., Vech, D., & Kasper, J. 2018, PhRvL, 120, 205102
Klein, K. G., Kasper, J. C., Korreck, K., & Stevens, M. L. 2017, JGRA, 122, 9815
Liu, Y. C.-M., Lee, M. A., & Kucharek, H. 2005, JGRA, 110, A9
Liu, Y. C.-M., Lee, M. A., Kucharek, H., & Miao, B. 2007, JGRA, 112, A07217
Marsch, E. 1991, in Physics of the Inner Heliosphere II: Particles, Waves and Turbulence, ed. R. Schwenn & E. Marsch (Berlin: Springer), 45
Marsch, E., Ao, X.-Z., & Tu, C.-Y. 2004, JGRA, 109, 4102
Marsch, E., Goertz, C., & Richter, K. 1982, JGRA, 87, 5030
Marsch, E., & Goldstein, H. 1983, JGRA, 88, 9933
Marsch, E., Muehlhaeuser, K., Rosenbauer, H., & Schwenn, R. 1983, JGRA, 88, 2982
Martinović, M. M., Klein, K. G., Kasper, J. C., et al. 2020, ApJS, doi:10.3847/1538-4365/ab527f
Maruca, B., & Kasper, J. 2013, AdSpR, 52, 723
Maruca, B., Kasper, J., & Bale, S. 2011, PhRvL, 107, 201101
Maruca, B. A., Kasper, J. C., & Gary, S. P. 2012, ApJ, 748, 137
Matteini, L., Hellinger, P., Goldstein, B. E., et al. 2013, JGRA, 118, 2771
Matteini, L., Landi, S., Hellinger, P., et al. 2007, GeoRL, 34, L20105
Ogilvie, K., Chornay, D., Fritzenreiter, R., et al. 1995, SSRv, 71, 55
Perrone, D., Stansby, D., Horbury, T., & Matteini, L. 2018, MNRAS, 483, 3730
Richardson, I., Cliver, E., & Cane, H. 2002, JGRA, 107, 1304
Stansby, D., Perrone, D., Matteini, L., Horbury, T., & Salem, C. 2019, A&A, 623, L2
Tu, C.-y. 1988, JGRA, 93, 7
Wilson, L. B., III, Chen, L.-J., Wang, S., et al. 2019a, ApJS, 243, 8
Wilson, L. B., III, Chen, L.-J., Wang, S., et al. 2019b, ApJS, 245, 24